


RESEARCH ARTICLE

Open Access



# Performance assessment of activated carbon thermally modified with iron in the desulfurization of biogas in a static batch system supported by headspace gas chromatography

Mayerlin Edith Acuña Montaño<sup>1</sup>, Luciane Effting<sup>2</sup>, Carmen Luisa Barbosa Guedes<sup>2</sup>, Gregorio Guadalupe Carbajal Arizaga<sup>3</sup>, Renata Mello Giona<sup>4</sup>, Patricia Hissae Yassue Cordeiro<sup>5</sup>, César Ricardo Teixeira Tarley<sup>2</sup> and Alesandro Bail<sup>1\*</sup> 

## Abstract

A static batch arrangement composed of anti-leak vials coupled to gas chromatography is proposed as a complementary system for performance assessment of biogas desulfurization by adsorption. For testing, a modified commercial activated carbon produced by controlled thermal treatment in the presence of iron(III) species improved biogas desulfurization. The adsorbents showed a superior hydrogen sulfide removal compared to ordinary one. Pseudo-first-order, pseudo-second-order, and Bangham's kinetic models were used to fit experimental data. All studied samples followed pseudo-first-order model, indicating the predominance of physisorption, and Bangham's model, confirming that the micropores structure played an important role for gases diffusion and adsorbent capacity. Additionally, the materials were characterized by N<sub>2</sub> adsorption-desorption, X-ray diffraction, infrared spectroscopy, scanning electron microscopy and energy-dispersive spectroscopy. The thermal treatment associated with iron impregnation caused significant modifications in the surface of the materials, and the iron species showed two main benefits: an expressive increase in the specific area and the formation of specific adsorption sites for hydrogen sulfide removal. The results reinforce the advantages of iron-modified adsorbents in relation to their non-modified counterparts. The analytical methodology based on the confinement of multiple gases contributes to improving the understanding of the hydrogen sulfide adsorption process using pressure swing adsorption technology.

**Keywords** Desulfurization, Activated carbon, Adsorption, Biogas, Hydrogen sulfide

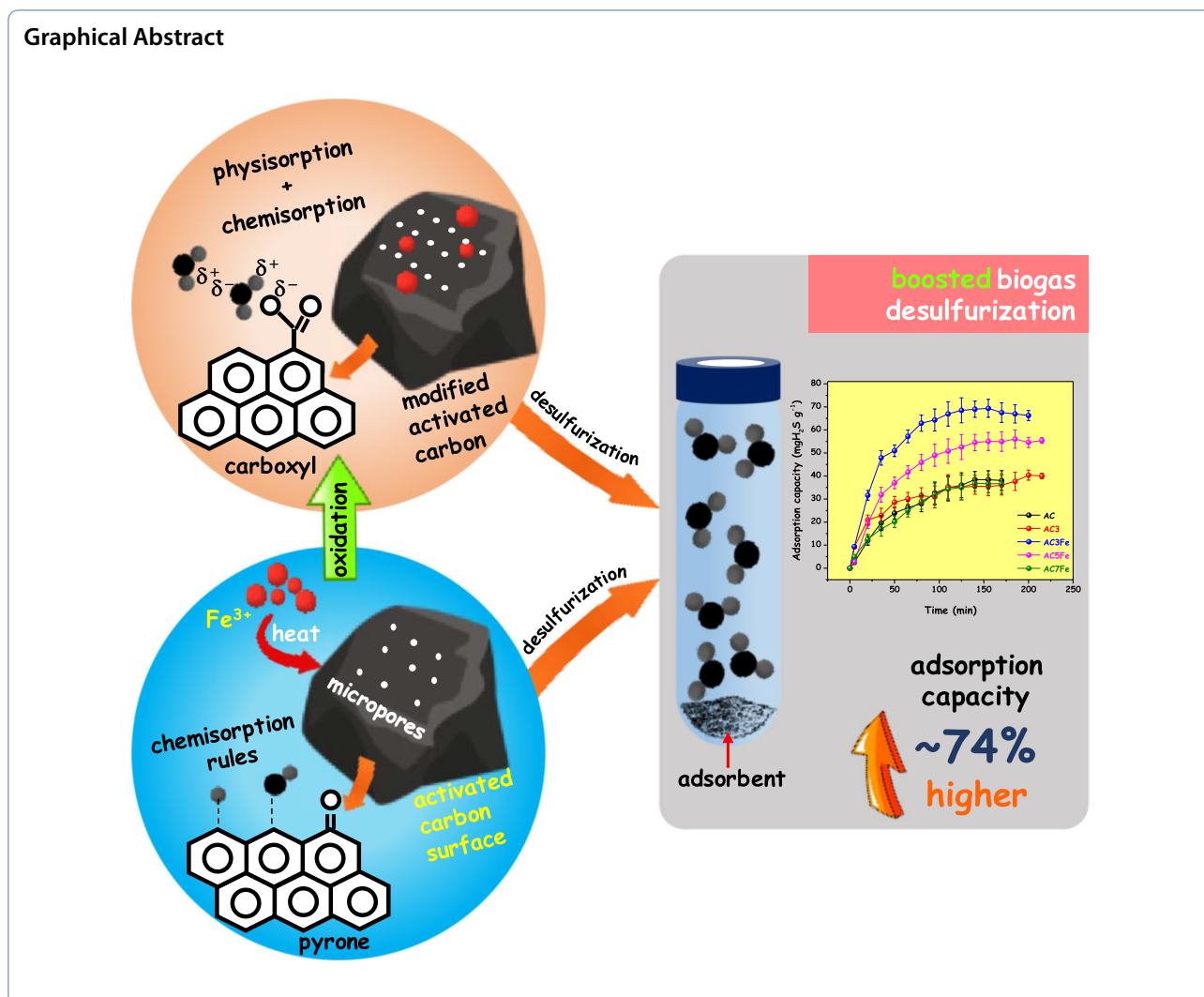
\*Correspondence:

Alesandro Bail  
alebail@utfpr.edu.br

Full list of author information is available at the end of the article



© The Author(s) 2024. **Open Access** This article is licensed under a Creative Commons Attribution 4.0 International License, which permits use, sharing, adaptation, distribution and reproduction in any medium or format, as long as you give appropriate credit to the original author(s) and the source, provide a link to the Creative Commons licence, and indicate if changes were made. The images or other third party material in this article are included in the article's Creative Commons licence, unless indicated otherwise in a credit line to the material. If material is not included in the article's Creative Commons licence and your intended use is not permitted by statutory regulation or exceeds the permitted use, you will need to obtain permission directly from the copyright holder. To view a copy of this licence, visit <http://creativecommons.org/licenses/by/4.0/>.



## Introduction

Hydrogen sulfide (H<sub>2</sub>S) is one of the most harmful contaminants of biogas, and its removal is mandatory to produce safe and sustainable biofuels based on renewable hydrocarbons. The main reasons for this are its high potential to cause severe corrosion in pipelines and metallic equipment, and the significant amount of sulfur oxides (SO<sub>x</sub>) that can be released into the atmosphere during the combustion of H<sub>2</sub>S-containing gaseous mixtures (Becker et al. 2022).

The biogas composition is quite variable and depends on the type of biomass used in the anaerobic digestion process (Calbry-Muzyka et al. 2022); however, in any case, H<sub>2</sub>S is the primary source of sulfur in biogas, and its level usually ranges from 700 to 2,000 ppmv but can reach up to 20,000 ppmv (Dumont 2015; Egger et al. 2023).

The European Committee of Standards specifies that biomethane, which is a gas with methane content usually higher than 90%, should have an H<sub>2</sub>S concentration <20 ppmv or ~0.0015% (vol/vol) (Okoro and Sun 2019), as well as the Brazilian Agency for Oil, Natural Gas and Biofuels (ANP) determines that the maximum limit for H<sub>2</sub>S in biomethane is 10 ppmv (ANP, Resolution n° 685/2017). In fact, some technologies compatible with (bio)methane require very low concentration of impurities, such as solid oxide fuel cells (SOFCs), in which the previous removal of volatile organic compounds (VOCs), from sulfur species to aromatic, chlorine and siloxane compounds, is mandatory in order to maximize the reliability of the equipment and increase its long-term service life (Illathukandy et al. 2022; Papurello et al. 2018; Zhu et al. 2020).

Therefore, raw biogas is typically submitted to a refining process to remove impurities and meet quality

standards. This process is usually divided into two steps: a cleaning step, in which  $H_2S$ ,  $H_2O$ , VOCs, siloxanes and other minor impurities are removed from the biogas (Calbry-Muzyka et al. 2022; Lecharlier et al. 2022; Tiwari et al. 2022), and an upgrading step, in which carbon dioxide, the primary contaminant, is removed to increase the methane content and raise the heat value of the biofuel (Pinto et al. 2022). Although siloxanes and other minor compounds are also potentially corrosive to metal components and can cause lubricant leaks (Boldrin et al. 2016; Illathukandy et al. 2022; Papurello et al. 2019), the concern with  $H_2S$  is relatively greater mainly due to its high concentration.

Cleaning and upgrading of biogas are usually supported by four technologies: pressure swing adsorption (PSA), water/chemical scrubbing, membrane separation, and cryogenic distillation (Barbera et al. 2019). Additionally, membrane biofilm or microorganism-based filters can be used instead of physicochemical approaches, or even in association with them, to maximize the efficiency of the desulfurization step, despite its limitations due to the fragility of the microorganisms (Dumont 2015).

The choice of technology depends on several factors, such as the type of biomass available for anaerobic digestion, specific biomethane end-use segment, and even the producer's investment capacity (Ardolino et al. 2021). Nonetheless, many biogas producers, on both small and large scales, use pressure swing adsorption technology or fixed bed columns stuffed with an adsorbent material and operating at room pressure for biogas cleaning and upgrading. Adsorption processes rule these two cases, and the surface of the filling material must have high capacity and selectivity for a given target contaminant.

Depending on the interaction strength between the target and the sorbent surface, the adsorption processes can occur by physisorption or chemisorption. While in physisorption, the sorbate and sorbent interact by weak forces and allow a more straightforward regeneration, in chemisorption, this interaction involves more energy and is generally irreversible (Bezerra et al. 2011).

Activated carbon (AC) is employed as an adsorbent for molecules and ions, both in gaseous and liquid systems. AC is obtained from chemical or physical activation of the biochar, which is the solid portion resultant from the pyrolysis of lignocellulosic biomass (Indayaningsih et al. 2017; Qu et al. 2018). Usually, AC shows a high surface area, good commercial availability, and relatively low cost, which are significant advantages for biogas refining worldwide (Sinha et al. 2020).

Its surface properties, such as surface charge distribution, functional group availability, pore size, and specific surface area, are directly correlated with  $H_2S$  removal from biogas (Zulkefli et al. 2023). An accepted

mechanism for  $H_2S$  removal by AC is based on the direct reaction between oxygen-containing groups localized on the AC surface and  $H_2S$  molecules to form oxidized elemental sulfur due to the presence of pyrone groups (Bian et al. 2019). Therefore, researchers have sought to increase the reactive sites in AC to overcome the  $H_2S$  fluctuations generated in the anaerobic digestion that demands a longer-term fixed-bed column in order to minimize stoppages for adsorbent replacement (Ou et al. 2020).

An adsorbent with a large capacity would lead to fewer operational stoppages for changing the column packing, and the producer's profit could be positively impacted if biogas processing had fewer interruptions. At least for the small biogas producers worldwide, an adsorbent such as AC, with enhanced capacity for  $H_2S$  removal, would be essential.

A systematic strategy to increase the adsorption capacity of materials has been to focus on modifying the AC surface by impregnation with chemical species of high affinity for  $H_2S$ , such as iron, zinc, copper, and other metal-based compounds (Barroso-Bogeat et al. 2019; Choudhury and Lansing 2021).

Like other d-block metals, iron presents an outstanding thermodynamic energy to adsorb  $H_2S$ . Therefore, an intuitive strategy has been to promote the contact between metal-containing materials and biogas, aiming at its purification (Cheremisina et al. 2022). For instance, Choudhury and Lansing (2021) synthesized two carbon-based biosorbents under 500 °C and promoted their impregnation with iron(III) chloride from an aqueous solution. The  $H_2S$  adsorption capacity in the fixed-bed column increased by 2.5–3.9 compared to the unmodified one. Cimino et al. (2020) developed a CuO–ZnO mixture dispersed onto commercial activated carbon, oxidizing  $H_2S$  to form sulfates or elemental sulfur. According to the authors, the presence of  $O_2$  or  $H_2O$  favors oxidative reaction and the formation of elemental sulfur on copper sites but not in zinc ones. On the other hand, sulfate species are predominant in the absence of oxygen or moisture, and they are formed utilizing lattice oxygen from metal oxide clusters or superficial oxygen species.

Another aspect that has been extensively addressed is related to functional groups on the AC surface and their role in  $H_2S$  adsorption. Shen et al. (2019) performed a density functional theory (DFT) study and found that groups such as carbonyl, ester, and, preferably, pyrone present an important effect on  $H_2S$  adsorption. Pyrone groups are considered basic and are produced by exposing heat-treated activated carbon to air. Authors inferred that the combination of carbonyl and epoxy oxygen atoms from the pyrone group creates an appropriate chemical

environment for dissociating H<sub>2</sub>S and its adsorption on pyrone groups predominantly ruled by chemisorption with a highly exothermic adsorption enthalpy.

These examples depict that modifying carbon-based materials by d-block metals and thermal treatment are important strategies to enhance adsorption-based technologies, i.e., PSA and fix-bed columns, to meet biogas production standards. In any adsorption case, the assessment of the mass capacity of the adsorbent material is crucial for process planning and viability.

In this work, a static batch system composed of anti-leak vials were used for gas confinement in order to evaluate the synthetic biogas desulfurization by headspace gas chromatography using a thermal conductivity detector. The studied adsorbent was a commercial activated carbon impregnated with iron species and submitted to thermal treatment to boost its performance.

## Experimental

### Chemicals

A typical activated carbon commercially available, obtained from a eucalyptus plant from a Brazilian reforestation area, granule size lower than 0.044 mm (50–70 wt%). Iron(III) chloride hexahydrate, FeCl<sub>3</sub>·6H<sub>2</sub>O, purity > 97 wt% was purchased from Synth; Nitric acid (HNO<sub>3</sub>) purity 63 wt% was purchased from Neon. A synthetic biogas mixture containing methane (CH<sub>4</sub>) 60.0% (vol/vol), carbon dioxide (CO<sub>2</sub>) 39.70% (vol/vol), and hydrogen sulfide (H<sub>2</sub>S) 3,000 ppmv (0.3% (vol/vol) or 4181.6 mg m<sup>-3</sup> at 298.15 K) was supplied by White Martins. The gaseous mixture was stored in a high-pressure aluminum cylinder (ALC type) at approximately 9.5–10.0 MPa. The other gases for chromatography were helium (He), hydrogen (H<sub>2</sub>), and nitrogen (N<sub>2</sub>), with purity 99.999%. The diluent sodium chloride (NaCl), purity 98.5 wt%, was purchased from Neon; Potassium thiocyanate (KSCN), purity > 98.5 wt%, was purchased from Dinamica. A standard solution of Fe<sup>3+</sup> (999 ± 5 mg L<sup>-1</sup>) was purchased from SpecSol. All reagents and gases were used without any treatment.

### Preparation of the adsorbents

Adsorbents were prepared by impregnation with FeCl<sub>3</sub>·6H<sub>2</sub>O and thermal treatment. The activated carbon (AC) was impregnated with iron according to the method described by Choudhury and Lansing (2021) with slight modifications. In brief, approximately 2.0 g of AC was added to an Erlenmeyer flask containing 60 mL of a 1000 mg L<sup>-1</sup> of Fe(III) dissolved in 1.0% (vol/vol) HNO<sub>3</sub> aqueous solution. The magnetic stirring (~500 rpm) was controlled from 5 to 300 min. Afterward, the impregnated AC was filtered using a 0.45 μm nylon syringe filter without washing to maximize iron ions availability during

the thermal treatment step. The supernatant was analyzed by UV–Vis spectroscopy to monitor the iron(III) ions concentration through the formation of the complex red pentaqua(thiocyanate)iron(III) [Fe(NCS)(OH<sub>2</sub>)<sub>5</sub>]<sup>2+</sup>, detected at λ<sub>max</sub> = 460 nm.

For the calculation of the iron(III) concentration remaining in the supernatant, a calibration curve with the dynamic range of 1.0–10.0 mgFe<sup>3+</sup> L<sup>-1</sup> and Eq. 1 was considered:

$$q_e = \frac{[(C_0 - C_1)V]}{m} \quad (1)$$

in which q<sub>e</sub> is the maximum adsorption capacity (mgFe g<sup>-1</sup>); C<sub>0</sub> is the initial concentration of Fe(III) (mg L<sup>-1</sup>); C<sub>1</sub> is the concentration of Fe(III) at equilibrium (mg L<sup>-1</sup>); V is the volume of Fe(III) aqueous solution (L); and m is the mass of AC (g).

Then, a portion of each material was dried at 100 °C for 4 h and treated in a muffle furnace at different temperatures (300, 500, and 700 °C) for 60 min with a thermal increment of 10 °C min<sup>-1</sup>. Upon controlled cooling in a desiccator, the samples were stored and labeled AC3Fe, AC5Fe, and AC7Fe, referring to the thermal treatment at 300, 500, and 700 °C, respectively. A sample labeled AC (commercial activated carbon submitted only to drying at 100 °C for 60 min for moisture removal) was considered a reference for the desulfurization tests. For language standardization purposes, in this work, a treated material means chemically or thermally treated; therefore, it does not comprise a simple drying to remove moisture. An additional material labeled AC3 was obtained by thermal treatment of the AC at 300 °C for 60 min without previous impregnation with iron.

### Equipment for analysis and characterization

Powder X-ray diffraction analysis (PXRD) was conducted in a Bruker D2 Phaser diffractometer operating at 30 kV and 40 mA with copper radiation (Cu–Kα = 0.15418 nm) in the range 10–75° with dwell a time of 2° min<sup>-1</sup>.

Scanning electron microscopy (SEM) and energy-dispersive spectroscopy (EDS) were recorded in an FE-SEM TESCAN model VEGA 4, corresponding to a tungsten thermionic emission system. The measurements were conducted at 15–30 kV acceleration potential under a high vacuum. The surfaces of the samples were coated with gold (sputtering—Denton Vacuum Desk V, using a current of 30 mA for 2 min). The absorption peaks due to the gold layer were attenuated in the data processing software Tescan Essence.

Attenuated total reflectance-Fourier transform infrared (ATR-FTIR) spectra were registered on a PerkinElmer spectrometer model Spectrum Two in the range



400–4000  $\text{cm}^{-1}$ . The spectra were collected with a resolution of 4  $\text{cm}^{-1}$  and an accumulation of 16 scans.

Adsorption/desorption of  $\text{N}_2$  analysis was performed to measure the specific surface area, the average pore diameter, and the pore volume of the ACs. For this purpose, the BET (Brunauer et al. 1938) and the BJH (Barret et al. 1951) methods were applied to the corresponding nitrogen desorption isotherms. The method de Boer (De Boer et al. 1966) was used for micropore and external area calculations. Data were collected on an ASAP 2020 N Automatic Physisorption Analyzer from Micrometrics at 77 K. The samples were previously degassed by treatment at 150 °C until the system pressure had achieved 10  $\mu\text{mHg}$ . The nitrogen adsorption data were obtained using approximately 0.1 g of the sample.

UV–Vis analysis was carried out on a spectrophotometer Biochrom model S60 Libra at  $\lambda_{\text{max}} = 460 \text{ nm}$  with a resolution of 2 nm.

Gas chromatography (GC) was used to determine  $\text{H}_2\text{S}$  using experimental parameters according to the column supplier (Agilent 2023). An equipment Agilent model 7820A, equipped with a thermal conductivity detector (TCD) and an HP-Plot Q column, 0.53 mm  $\times$  30 m, was employed in the experiments. The main conditions of analysis were: carrier gas He, flow rate 8.6  $\text{mL min}^{-1}$ ; oven temperature 60 °C; initial temperature ( $T_i$ ) 60 °C (by 2 min), temperature rate 30 °C  $\text{min}^{-1}$ , final temperature ( $T_f$ ) 240 °C (by 1 min); the temperature of the detector 250 °C; splitless injection mode; sample volume 250  $\mu\text{L}$ .

### Desulfurization experiments

$\text{H}_2\text{S}$  removal from the gaseous mixture (synthetic biogas) was evaluated in static batch experiments, and the analytical steps are depicted in Fig. 1. Although the continuous flow approach in a fixed bed column can be a better way to represent the most used operational processes, the capacity of  $\text{H}_2\text{S}$  removal of the samples could be determined in batch experiments, which represents, in a simplified way, the mass transfer equilibrium expected in a PSA system. In addition, this approach can allow a significant cost reduction owing to the lower consumption of synthetic gaseous mixture.

For the experiments, all samples were grounded in a ceramic mortar, sieved in the range, 0.044–0.063 mm followed by drying at 100 °C for 60 min and cooling down to room temperature in a vacuum desiccator. Each sample was diluted before weighing by a factor of a hundred (10.0 mg of sample to 1.0 g of diluent) by addition of powdered dry sodium chloride to enable weighing in a reliable range of the analytical balance with resolution of 0.1 mg (Ohaus PR224BR/E). Both sample and diluent were placed together in a flask with a lid and vigorously shaken until a homogeneous greyish mixture was formed.

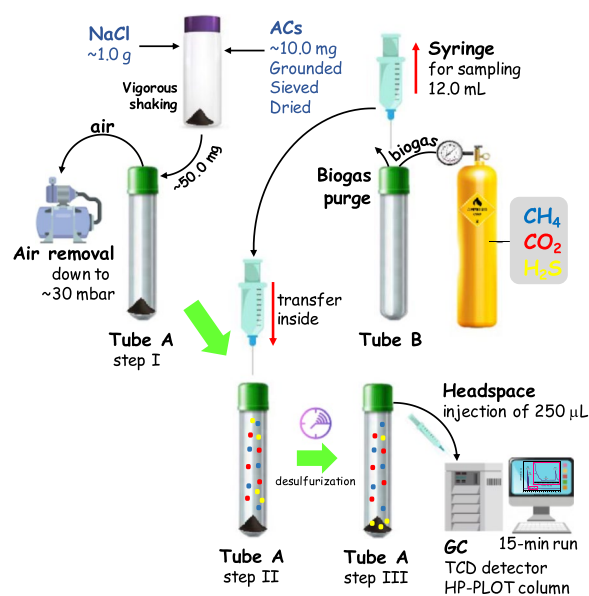


**Fig. 1** Schematic representation of the steps considered in the materials assessment during adsorption of  $\text{H}_2\text{S}$  from synthetic biogas

Afterward, 50.0 mg of the diluted material was weighed in a 12-mL glass tube purchased from Labco Exetainer sealed with plastic screw-caps containing chlorobutyl septum (anti-leak vials). The air pressure inside the tube was lowered to  $\sim 3.0 \text{ kPa}$  for 1 min with a vacuum pump (Tube A). In parallel, another sealed tube (Tube B) had its internal content purged by a gentle stream of synthetic biogas. After a few seconds, 12.0 mL of synthetic biogas were carefully sampled during the purge to ensure room pressure stability and immediately transferred to Tube A. The contact time between diluted materials and synthetic biogas started to be registered, and the adsorption process was monitored with periodic headspace sampling in intervals of 15 min using a 250- $\mu\text{L}$  gastight syringe by gas chromatography until the  $\text{H}_2\text{S}$  concentration remained constant for at least three consecutive chromatographic runs. A blank test was performed following the same protocols described above, however, using an excess of 50.0 mg of the diluent (NaCl) in a control tube to prove the diluent's inertia. For this reason, some aliquots were taken from the control tube for GC analysis after 250 min of contact with the synthetic biogas.

The calculations of maximum adsorption capacity ( $q_{\text{H}_2\text{S}}$ ) were carried out considering the ideal gas behavior of the gaseous mixture with initial pressure  $\sim 101.3 \text{ kPa}$  and constant temperature at 25 °C (298.15 K), which was possible in an air-conditioned room. According to Clapeyron's equation for ideal gases, the pressure inside the tube must decrease with decreasing number of moles of the gaseous mixture, which is expected to have happened

after each new aliquot withdrawn from the tube. From the difference between the initial and remaining ratio between area of chromatographic peaks of H<sub>2</sub>S and total gases, it was possible to calculate the mass of H<sub>2</sub>S adsorbed on the evaluated materials according to Eq. (2).

$$q_{\text{H}_2\text{S}} = \left\{ n_{\text{H}_2\text{Sinitial}} - \left[ \left( \frac{A_{\text{H}_2\text{S}}}{A_{\text{Total}}} \right)_{\text{react}} x \left( \frac{A_{\text{Total}}}{A_{\text{H}_2\text{S}}} \right)_{\text{std}} x n_{\text{H}_2\text{Sinitial}} \right] x MM \right\} / m_{\text{ads}} \quad (2)$$

in which  $q_{\text{H}_2\text{S}}$  is the adsorption capacity of H<sub>2</sub>S at equilibrium (mg g<sup>-1</sup>);  $n_{\text{H}_2\text{Sinitial}}$  = moles of H<sub>2</sub>S contained in 12.0 mL of standard gaseous mixture at 101.3 kPa and 298.15 K;  $\left( \frac{A_{\text{H}_2\text{S}}}{A_{\text{Total}}} \right)_{\text{react}}$  = ratio between area of H<sub>2</sub>S and total area of a given reaction;  $\left( \frac{A_{\text{H}_2\text{S}}}{A_{\text{Total}}} \right)_{\text{std}}$  = ratio between area of H<sub>2</sub>S and total area of the standard mixture; MM = molar mass of H<sub>2</sub>S (34,100 mg mol<sup>-1</sup>);  $m_{\text{ads}}$  = mass of adsorbent (g).

Analysis of variance test (ANOVA) with 95% confidence level was carried out on the results of performance. The null hypothesis was that the average of the H<sub>2</sub>S removal from synthetic biogas in the presence of the modified adsorbents would be the same.

#### Kinetic models assessment

The desulfurization experiments were assessed by three different nonlinear kinetic models: pseudo-first-order (PFO, Eq. 3), pseudo-second-order (PSO, Eq. 4), and Bangham's model (Eq. 5) (Georgiadis et al. 2021). For all cases, the iteration algorithm used was orthogonal distance regression, and the nonlinear forms of each model are displayed by Eqs. (3–5), as follows.

$$q_t = q_e \left( 1 - e^{-k_1 t} \right) \quad (3)$$

in which  $q_t$  and  $q_e$  are the amount of H<sub>2</sub>S adsorbed (mg g<sup>-1</sup>) at time  $t$  (min) and after equilibrium of adsorption, respectively;  $k_1$  is the pseudo-first-order rate constant (min<sup>-1</sup>);  $t$  is the elapsed time for the adsorption reaction (min).

$$q_t = \frac{q_e^2 k_2 t}{1 + q_t k_2 t} \quad (4)$$

in which  $q_t$  and  $q_e$  are the amount of H<sub>2</sub>S adsorbed (mg g<sup>-1</sup>) at time  $t$  (min) and after equilibrium of adsorption, respectively;  $k_2$  is the pseudo-second-order rate constant (g mg<sup>-1</sup> min<sup>-1</sup>);  $t$  is the elapsed time for the adsorption reaction (min).

$$q_t = q_e \left[ 1 - \left( e^{-k_b t^n} \right) \right] \quad (5)$$

in which  $q_t$  and  $q_e$  are the amount of H<sub>2</sub>S adsorbed (mg g<sup>-1</sup>) at time  $t$  (min) and after equilibrium of adsorption, respectively;  $k_b$  (min<sup>-n</sup>) and  $n$  are Bangham's constants;  $t$  is the elapsed time for the adsorption reaction (min).

## Results and discussion

### Preparation of the adsorbents

The iron concentration of the ACs was indirectly determined by UV–Vis spectroscopy analysis of the iron(III) ions remaining in the supernatant as [Fe(NCS)(OH)<sub>2</sub>]<sub>5</sub><sup>2+</sup> complex. This method was chosen instead of the direct determination of iron on the solid to avoid an underestimated result due to a possible difficulty to total solubilization of the iron by acidic digestion. Considering that the impregnated materials were not submitted to washing during their preparation, the difference between the concentration of iron(III) ions in the supernatant and the initial iron(III) concentration corresponds to the amount of iron adsorbed on the ACs. The AC showed a high affinity for iron(III) ions, and only 5 min was required to reach a high uptake from the acid solution. All the reaction times led to a similar iron content (average adsorption of 28.8 ± 0.20 mg of Fe by g of AC), representing 97.6 ± 0.25% of the total iron(III) ions available in the acid solution. Although there was no significant difference in iron load in ACs concerning reaction time, extended contact usually helps to create better control of experimental parameters in the impregnation system. In addition, the iron load was comparable to those obtained by Chang et al. (2010) and Kalaruban et al. (2019), who found values ranging from 19 to 26 mgFe g<sup>-1</sup> using granular activated carbon. Nevertheless, Martins et al. (2022) obtained a higher value, 178 mgFe g<sup>-1</sup>, using commercial activated carbon under strong acid conditions. These disparities indicate that iron impregnation has a high dependence on the experimental procedures, as well as on characteristics of the material used, such as specific area, pore size/volume, the intensity of the thermal treatment before the impregnation step, weight ratio metal/AC, among others.

An important consideration must be made regarding the iron load in each material after thermal treatment. Because mass loss was detected as the temperature was raised due to the thermal decomposition of activated carbon under an O<sub>2</sub>-rich atmosphere, an increase in the iron load in materials can be expected (Table 1). The mass loss of 15.1% depicted by AC3Fe was responsible for an estimated iron load increasing from 28.8 to 33.9 mg g<sup>-1</sup>. In

**Table 1** Iron loading estimate in the ACs after mass loss observed during thermal treatment

Sample ID	Mass loss <sup>a</sup> (%)	Iron loading <sup>b</sup> (mg g <sup>-1</sup> )
AC3Fe	15.1	33.9
AC5Fe	72.5	104.7
AC7Fe	79.0	137.1
AC	9.89	–

<sup>a</sup> Obtained by gravimetric analysis<sup>b</sup> Estimated according to mass loss during thermal treatmentThe initial iron content was 28.8 ± 0.20 mg Fe g<sup>-1</sup> by UV-Vis spectroscopy

addition, the sample AC3 (without iron) presented 9.89% mass loss after thermal treatment, confirming the role of the iron species in the modification of the carbonaceous materials. On the other hand, owing to the treatment intensity performed over AC5Fe and AC7Fe, these materials depicted a more substantial mass loss, reaching 72.5 and 79.0%, respectively, indicating intensive mineralization. Considering that the residence time in the muffle was relatively short (60 min), the thermal treatment may not have been able to decompose all the organic matter, leading to an increasing loading of iron in the presence of the remaining carbonaceous matrix, which reached 104.7 mgFe g<sup>-1</sup> for AC5Fe and 137.1 mgFe g<sup>-1</sup> for AC7Fe.

### Characterization of the modified ACs

Often, two crucial characteristics to consider for activated carbon applied to adsorption processes are a high specific area (high pore volume) and a well-formed pore structure. Table 2 shows that AC exhibited a specific area of 325.3 m<sup>2</sup> g<sup>-1</sup>, which is a little lower than the typical range reported by the literature for activated carbons 500–2000 m<sup>2</sup> g<sup>-1</sup> (Fahmi et al. 2019), as well as compared to the exceptional areas that this type of material can reach (~3500 m<sup>2</sup> g<sup>-1</sup>) if the synthesis conditions are optimized (Ma et al. 2020). Additionally, AC showed 172.8 m<sup>2</sup> g<sup>-1</sup> (53% of the total area), referring

to micropores ( $S_{\text{micro}}$ ) and 153.0 m<sup>2</sup> g<sup>-1</sup> (47.1% of the total area), referring to the external area ( $S_{\text{ext}}$ ), which is interpreted as the available area outside the pores. The average pore size was 1.53 nm, confirming the predominance of micropores, and the average pore volume was 0.25 cm<sup>3</sup> g<sup>-1</sup>. Table 2 shows that the increase in the temperature of the thermal treatment up to 300 °C under air led to a remarkable increase in the specific area, with AC3 reaching 479.9 m<sup>2</sup> g<sup>-1</sup>, accompanied by a slight decrease of its average pore size (1.36 nm), and an increase of its pore volume (0.32 cm<sup>3</sup> g<sup>-1</sup>). Considering the different pore size distributions and morphologies possible in activated carbon, including conical-shaped pores, these results suggest that the thermal treatment caused an abrasion on the surface of the activated carbon particles, exposing regions with smaller opening micropores. Moreover, new micropores may also have appeared. The gain in the specific area was even more evident for AC3Fe material (533.4 m<sup>2</sup> g<sup>-1</sup>, 64 wt% higher than AC), which was treated in the presence of iron species. Its average pore size (1.37 nm) was too close to those presented by AC3; however, its pore volume was slightly higher than for AC3, indicating that despite the 15.1% mass loss (Table 1), the iron species contributed to the formation of new pores and deepening of the existing ones. The thermal treatment at 500 °C for AC5Fe did not cause a significant decrease in its  $S_{\text{BET}}$  (317.2 m<sup>2</sup> g<sup>-1</sup>) and its pore volume (0.22 cm<sup>3</sup> g<sup>-1</sup>) in comparison with AC; it seems that the high mass loss (72.5 wt%) had been offset by the gain in porosity. Conversely, a significant drop at higher temperatures was observed for AC7Fe, with the total specific area ( $S_{\text{BET}}$ ) decreasing to 236.6 m<sup>2</sup> g<sup>-1</sup> and pore volume to 0.17 cm<sup>3</sup> g<sup>-1</sup>. Moreover, the decrease in  $S_{\text{ext}}/S_{\text{BET}}$  ratio presented by modified ACs (from 47.1 to ~30%), and consequently, the increase in  $S_{\text{micro}}/S_{\text{BET}}$  ratio (from 53.1 to ~70%), occurred due to the appearance of micrometric pores, depicted in Fig. 3 (see SEM analysis), of an exceptionally large size of about ~5–15 μm. The walls of these “big pores” are expected to be full of interconnected

**Table 2** Textural parameters obtained for the materials, including micropore, external and BET specific areas, average pore size and average pore volume

ID	$S_{\text{micro}}^b$ (m <sup>2</sup> g <sup>-1</sup> )	$S_{\text{ext}}$ (m <sup>2</sup> g <sup>-1</sup> )	$S_{\text{BET}}^a$ (m <sup>2</sup> g <sup>-1</sup> )	Average pore size <sup>c</sup> (nm)	Average pore volume <sup>c</sup> (cm <sup>3</sup> g <sup>-1</sup> )
AC	172.8	153.0	325.3	1.53	0.25
AC3Fe	378.2	155.8	533.4	1.37	0.36
AC5Fe	225.6	92.9	317.2	1.37	0.22
AC7Fe	162.1	74.5	236.6	1.43	0.17
AC3	343.5	136.4	479.9	1.36	0.32

Determined by <sup>a</sup>BET method, <sup>b</sup>de Boer method and <sup>c</sup>BJH method

micropores (<2 nm), originally blind and closed pores, which were connected due to the intense abrasion caused by the combination of high temperature and iron species. In general, the average pore volume was directly proportional to the specific area of the materials.

All nitrogen adsorption–desorption isotherms registered at 77 K showed a similar profile (Fig. 2). All isotherms were classified as Type I, referring to a micropore-containing material (Pires et al. 2021); however, the hysteresis loop type H4 seen ranging from  $P/P_0$  0.45 to 0.92, that usually arises from capillary condensation, indicates the existence of additional small mesopores forming a heterogeneous porous matrix (Blåker et al. 2019). The insets in Fig. 2 show the average pore size in alignment with the results presented in Table 2, which means a predominance of micropores and small mesopores.

SEM analysis aids in comprehending the surface characteristics of a given material proposed as an adsorbent and its adsorption dynamic. Therefore, information about roughness and agglomeration, mainly the existence of pores, their shape, size, and distribution over the surface of the particles, are fundamental to increase the adsorbent performance.

Figure 3a–j shows a set of images that depict the profile of ACs samples based on typical pyrolyzed biomass composed of graphite and probably a few contributions of unchanged cellulose fragments, in which lignin might remain stable even at about 900 °C (Waters et al. 2017). The first row of images (Fig. 3a–e) shows a comparison for at the same magnification (3kx), while the second row (Fig. 3f–j) shows some characteristic information about each material at different magnifications. The presence of cellulosic fragments is common to all materials, however in those thermal treated materials the mineralization process caused changes in the surface texture. Mineralization can be evidenced by the appearance of fracture and accumulation of small aggregates (Fig. 3b), as well as formation of macropores owing to the breakup of thinner pore walls already existing in the starting material (Fig. 3i). The images in Fig. 3c and h give a notion of the cross section of the cellulosic fragments in different directions. In both cases, the views allow to notice the massive presence of pores with ~10 µm in size; they are well organized and oriented parallel to each other along the analyzed fragment. The thermal treated material AC3 (without iron chloride) presented an accumulation of particles apparently inorganic in nature, with a degree of organization that resembles small quartz crystallites. Interestingly, the presence of these crystallites as well as the decrease in the availability of cellulosic fragments was more intense for the AC3 material than for the AC3Fe

material, suggesting that the iron chloride modifier has a relevant role during the thermal degradation of activated carbon.

Figure 4a–j shows the sample's EDS spectrum, element mapping, and weight fraction. As expected, the micrometric particles are predominantly formed by carbon. However, oxygen and silicon were found in all materials, suggesting the presence of a significant content of silicon oxide. For AC3Fe and AC5Fe, it was possible to detect iron and chlorine, which is in accordance with the starting material  $FeCl_3$ . The EDS mapping also shows that iron species are highly dispersed over the surface of the materials, and their content is lower than those obtained by UV–Vis (Table 1), which is typical for surface probing techniques such as EDS analysis. Another expected information is about the increase of the silicon content with the increase of the temperature used in the thermal treatment. Although EDS analysis results are highly dependent on the specific point of the analyzed particle and may not represent the bulk material, the image in Fig. 4g represents the accumulation of silicon oxide species. The particles chosen for scanning are the same as shown in Fig. 3g (SEM), showing the significant amount of silicon oxide species embedded in the carbonaceous matrix. Unlike AC3Fe, AC3 material did not present iron or chlorine in the EDS mapping; indeed, it showed a large predominance of carbon and a significant amount of silicon and oxygen as a result of the thermal decomposition of the carbonaceous matrix (Fig. 4i and j). The oxygen content increased from 6.04 wt% for AC (only dried at 100 °C) to 31.8 wt% for AC7Fe (700 °C), confirming that the ACs surface was strongly modified during the thermal treatment. Additionally, trace levels of certain elements such as aluminum (Al), potassium (K), and magnesium (Mg) were detected, which can be attributed to the typical composition of biomass. A persistent broad peak of relatively low intensity at ~2.1 kV referring to gold spectral line from samples metalization can be observe in all spectra after attenuation of unwanted signals. This peak was not accounted for centesimal composition.

In order to further characterize the materials, especially the presence of inorganic-thermally stable compounds and to enhance the comprehension on the role of the iron(III) chloride during the thermal treatment, the PXRD analysis was carried out, and the results are shown in Fig. 5. All samples presented diffraction peaks that stood out compared to the carbonaceous phase. The predominant signals were related to silica-based crystals, which agrees with the EDS results, indicating the presence of silicon and oxygen. Despite the high load of iron species (Table 1), it was impossible to identify diffraction peaks related to iron oxides or other iron crystalline



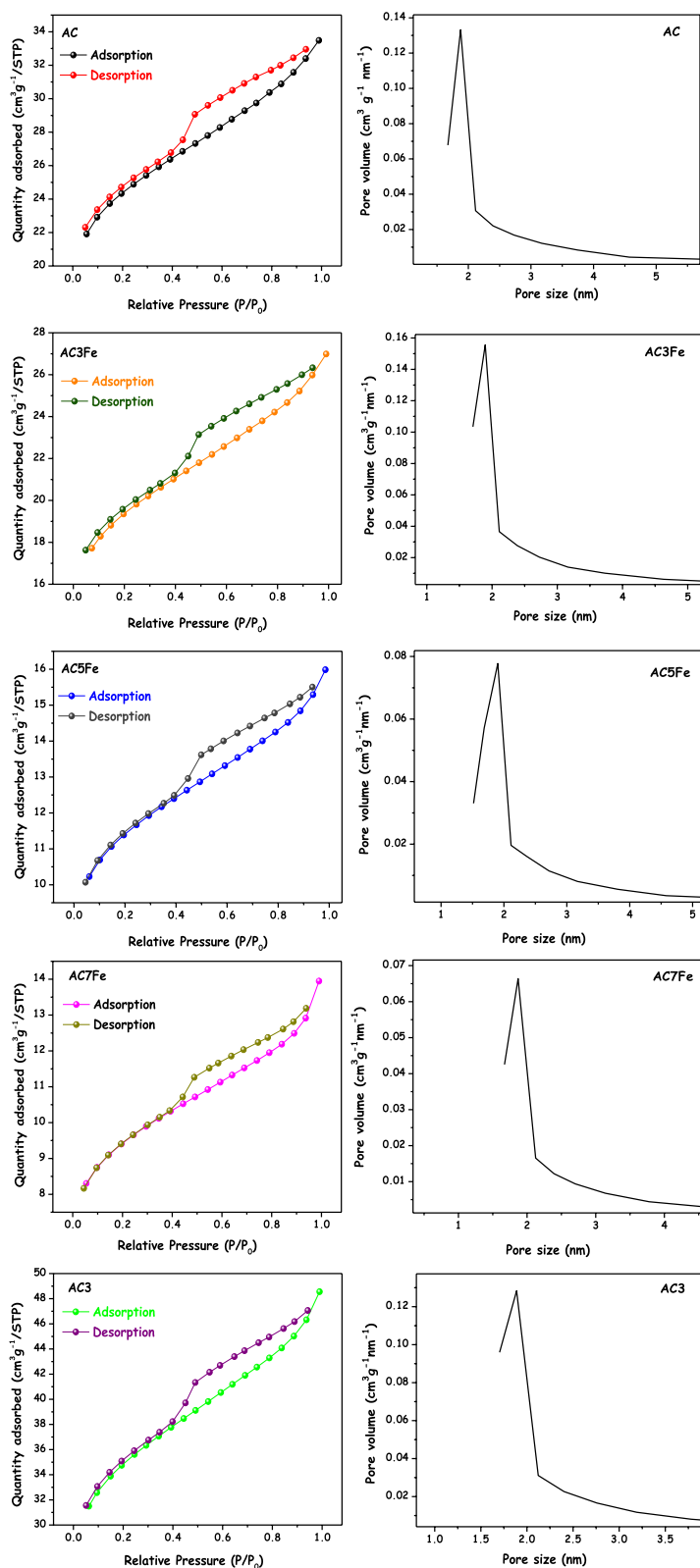


**Fig. 2** Nitrogen adsorption–desorption loops obtained for the evaluated materials at 77 K. The inset shows the pore size distribution remaining between micropores and small mesopores

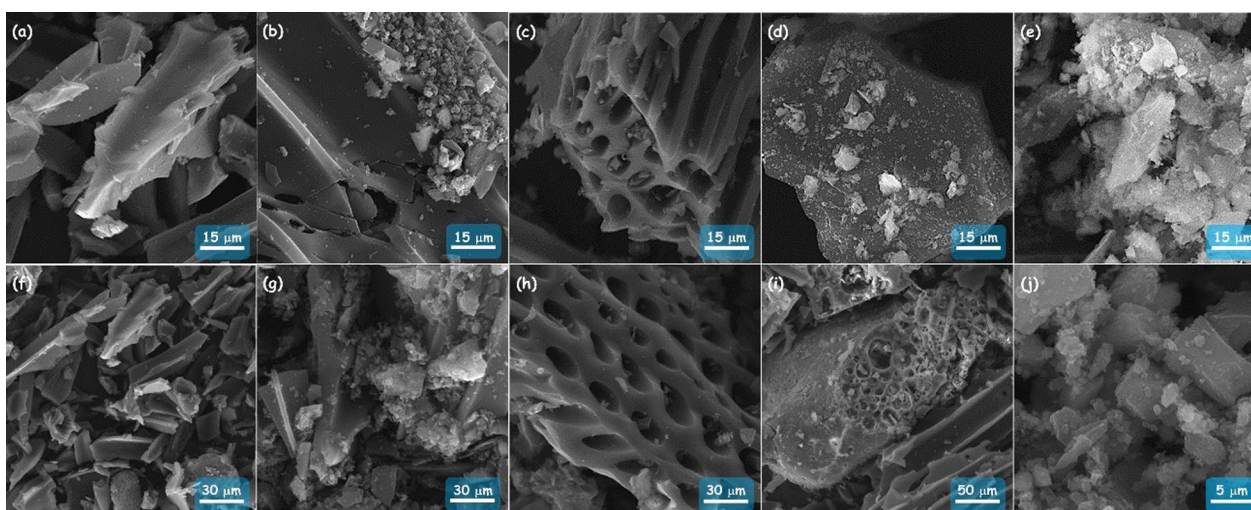


**Fig. 3** SEM images depicting the roughness of the surface of the studied materials AC (a, f), AC3Fe (b, g), AC5Fe (c, h), AC7Fe (d, i), and AC3 (e, j). The upper row shows comparative images for the materials at the same magnification scale (3kx). The down row shows some relevant details for each material under relevant magnification

phases, confirming that iron compounds may be highly dispersed onto the AC surface, avoiding crystallization.

The samples AC and AC3 presented some narrow diffraction peaks overlaying a discrete amorphous halo ranging from  $20$  to  $30^\circ$  ( $2\theta$ ). As a reference for the other materials, the diffraction peaks for AC were ticked by Q and assigned to quartz as follows:  $2\theta = 21.45^\circ$  (Q1),  $27.09^\circ$  (Q2), and  $36.81^\circ$  (Q3), referring to the planes (100), (101), and (200), respectively, according to ICSD Collection code 079634. Quartz can be considered a common inorganic impurity to biomass (Bhattacharjya and Yu 2014). Silicon from the soil converts into amorphous silica within the plant (Luyckx et al. 2017), forming crystalline phases under heating. Moreover, Yang et al. (2022) showed that silica-phase transformation could occur at lower temperatures than those widely reported, for instance, if metals or metal compounds are present. So, the peak at  $2\theta = 22.26^\circ$  was assigned to tridymite, a polymorph of silica stably formed above  $870^\circ\text{C}$  according to ICSD Collection code 408,281 (Li et al. 2021), which is a temperature usually reached in pyrolytic processes for activated carbon production.

Also, as expected for a carbon-based material, the presence of graphite is expected to be detected. As graphite usually shows an intense diffraction peak at  $2\theta = 26\text{--}27^\circ$  according to ICSD Collection code 031829 (Ganash et al. 2019), the peak at  $2\theta = 27.17^\circ$  in Fig. 5 was considered as overlapping between graphite and quartz signals, in which the former is partially hidden by the last. Despite that, a discrete splitting of this diffraction peak can be observed in sample AC5Fe due to long-range atomic order changes, shifting the graphite peak to  $2\theta = 26.6^\circ$ . In

addition, Fig. 5 shows that the thermal treatment allowed slight changes in crystallinity and the number of detectable peaks of quartz due to the intense decomposition of graphite and the gradual disappearance of the amorphous halo.

It is notable that, due to the thermal treatment at  $300^\circ\text{C}$ , the AC3 material presented relatively intense quartz-based peaks clearly higher than the AC, but nevertheless, also higher than the AC3Fe, whose thermal treatment was performed in the presence of iron(III) chloride. In addition, by inspection of Fig. 5, the profile of the AC3 is similar to that obtained for AC7Fe, which is known to have undergone a high degree of thermal decomposition and shows intense quartz peaks. As aforementioned, the iron(III) chloride played an important role in the production of modified activated carbons, resulting in more interesting textural properties, such as higher specific area, higher pore volume, increase of the microporosity, and deepening of pores. At the same time, iron(III) chloride seems to have mitigated the abrupt thermal decomposition of the ACs and promoted a controlled increase in porosity.

ATR-FTIR spectra of the materials are shown in Fig. 6. Although thermal treatment applied on the samples was enough to cause a significant mass loss, in general, the spectra show slight changes when the non-modified AC is compared to the other materials. Despite that, a remarkable change occurred in the region below  $1,000\text{ cm}^{-1}$ , in which the ACs treated at higher temperatures ( $500$  and  $700^\circ\text{C}$ ) presented two intense absorption bands centered at  $790$  and  $460\text{ cm}^{-1}$ . These bands can be related to stretches involving heavier atoms, such as

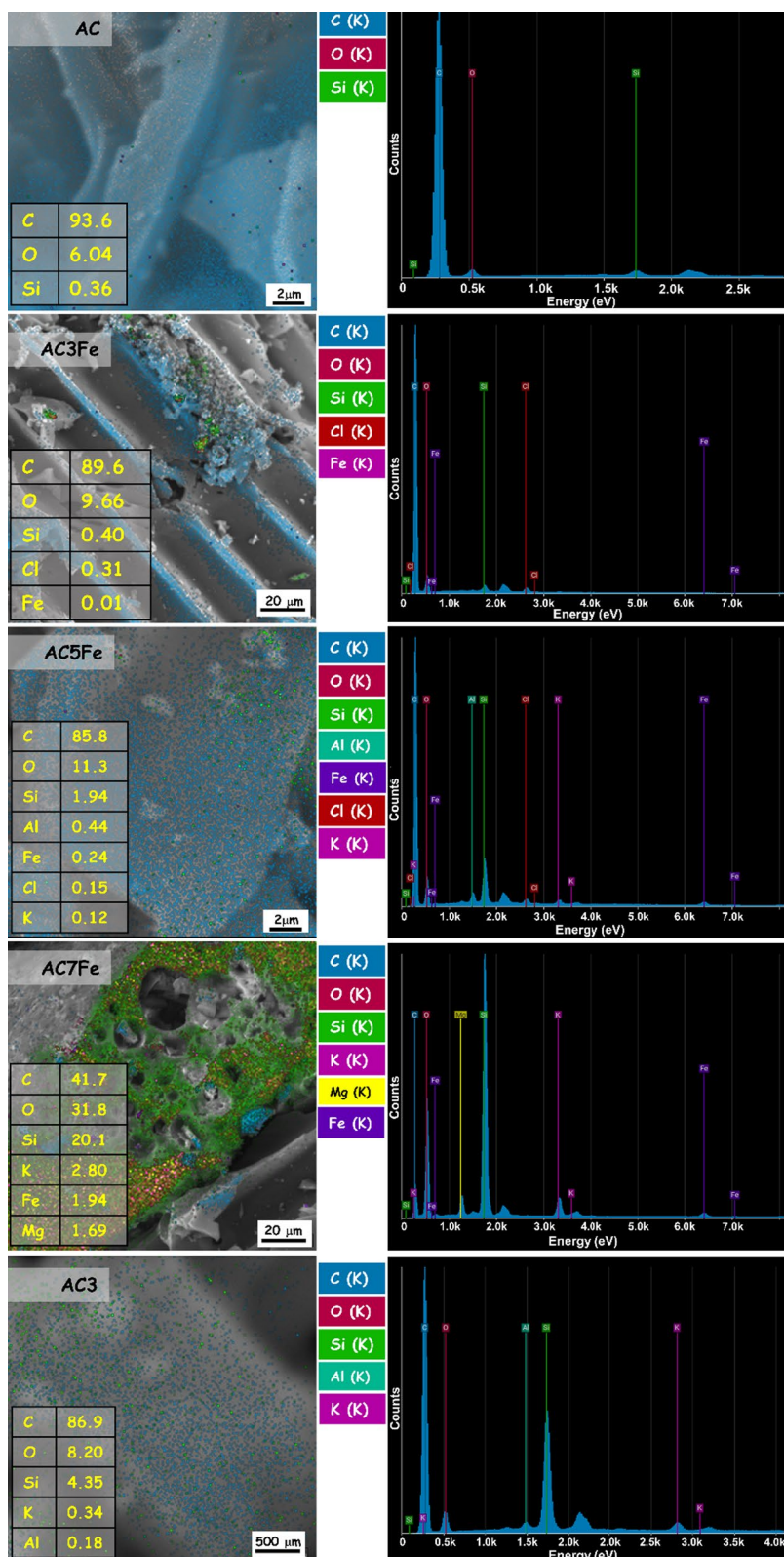


**Fig. 4** EDS results showing spectrum, element mapping and the weight fraction for each sample. Inset depicts the increase of the oxygen, silicon and iron contents as the thermal treatment temperature was raised

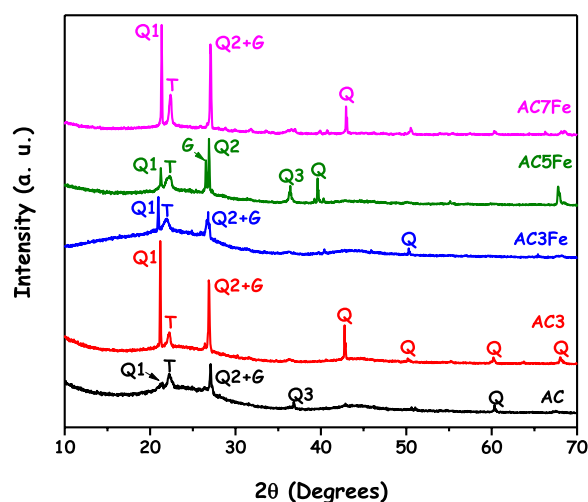


**Fig. 5** PXRD patterns of the evaluated materials evidencing the increase in quartz peak intensity with increase of the temperature

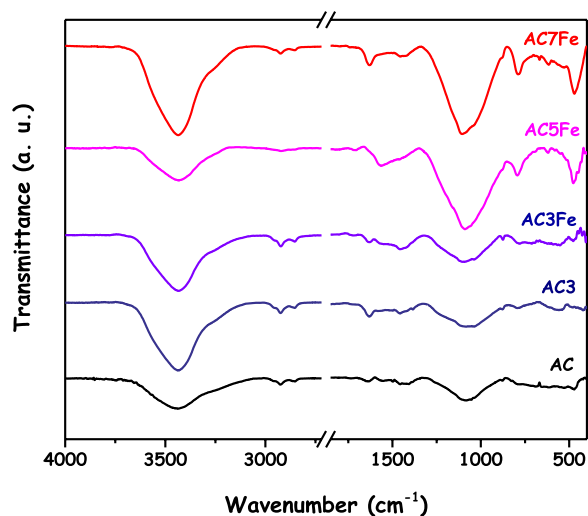


**Fig. 6** ATR-FTIR spectra of the produced materials evidencing the appearance of bands due to the presence of Fe–O stretches

those caused by Fe–O due to the decrease of the carbonaceous content during the thermal treatment. The other absorption bands are in accordance with the expected for activated carbon produced from vegetal biomass, including the broad absorption band centered at  $3450\text{ cm}^{-1}$ , which was attributed to O–H stretching modes from  $\text{H}_2\text{O}$  and hydroxyl groups. The counterpart bending mode absorption band from  $\text{H}_2\text{O}$  was detected at around  $1630\text{ cm}^{-1}$ . Alkyl structures of aliphatic groups, probably from a remaining portion of lignin, were evidenced by the set of absorption bands ranging from  $2969$  to  $2924\text{ cm}^{-1}$  and were assigned to  $\text{C}(\text{sp}^3)\text{-H}$  stretching modes (Waters et al. 2017). Moreover, the inorganic portion formed by

silicon compounds was identified by the broad absorption band centered at  $1090\text{ cm}^{-1}$ , assigned to Si–O vibration modes from siloxane (Si–O–Si), probably overlapped on a less intense band referring to silanol (Si–OH) groups. The significant content of silica depicted in ATR-FTIR spectra is in accordance with results obtained by PXRD and EDS.

#### Evaluation of the materials in desulfurization

The performance of the modified and non-modified ACs was comparatively assessed by adsorption batch experiments using a synthetic gaseous mixture composed of  $\text{CH}_4$ ,  $\text{CO}_2$ , and  $\text{H}_2\text{S}$ . The major gases (methane and carbon dioxide) had their concentrations practically constant throughout the experiments. Figure 7a shows five typical chromatograms obtained for the standard gaseous mixture sampled by the headspace technique and injected to monitor the GC system response, presenting an apparent profile of overlapping peaks and analytical repeatability. The average deviation calculated considering the area ratio of the peaks for these five injections of the standard mixture was 11.8%, which was considered a reasonable deviation for the experimental arrangement used. In the open-window image, it is possible to notice only the two peaks corresponding to major components,  $\text{CH}_4$  and  $\text{CO}_2$ , centered at 1.12 and 1.18 min, respectively, and a third peak attributed to  $\text{H}_2\text{O}$  centered at 3.21 min (Agilent 2023), which is expected due to small contamination of the system with atmospheric moisture during the sampling. The peak corresponding to  $\text{H}_2\text{S}$  centered at 2.44 min can only be observed in the inset of Fig. 7a owing to its relatively low concentration in the mixture. Although all peaks were detected before 5 min, each run was performed up to 9 min to ensure total elution of the components. These four peaks were considered for area integration. Figure 7b shows the decrease in the area ratio between  $\text{H}_2\text{S}$  and the total area along the batch adsorption experiments, with the curves presenting similar profiles but reaching a plateau at different levels. All materials were able to adsorb  $\text{H}_2\text{S}$ , resulting in a decrease in peak area ratio, including AC, AC3, and AC7Fe, with similar results, corresponding to 53.1, 55.6 and 49.3%, respectively. However, those ACs modified with iron and submitted to thermal treatment at 300 and  $500\text{ }^\circ\text{C}$  presented better performances in removing  $\text{H}_2\text{S}$ , with AC5Fe and AC3Fe reaching 83.9 and 97.8% of the decrease in their area ratios. These results reinforce the important role of the thermal treatment carried out in the presence of iron species. Additionally, the performance of the AC7Fe was affected by the excessive temperature applied to it, and the decrease in its specific area (Table 2) was responsible for a more discreet result. Nevertheless, the high iron content on the AC7Fe surface



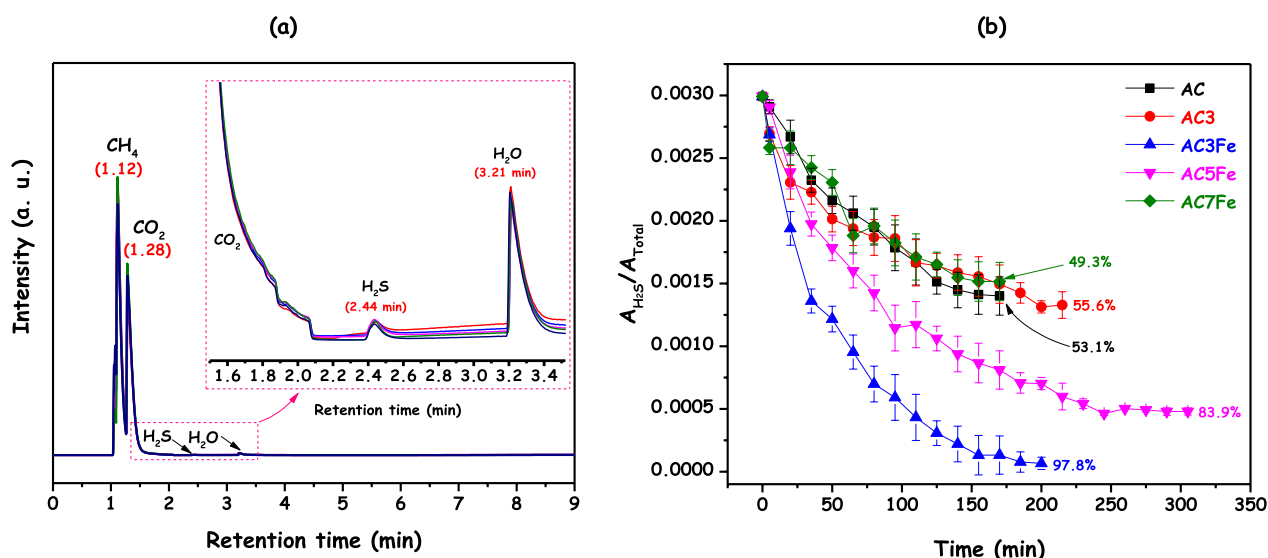


**Fig. 7** (a) GC chromatogram of the three-component gaseous standard mixture plus water from room moisture and their retention times. The inset shows the hydrogen sulfide peak. (b) Decrease in the area ratio evidencing the high capacity of  $\text{H}_2\text{S}$  adsorption on studied ACs

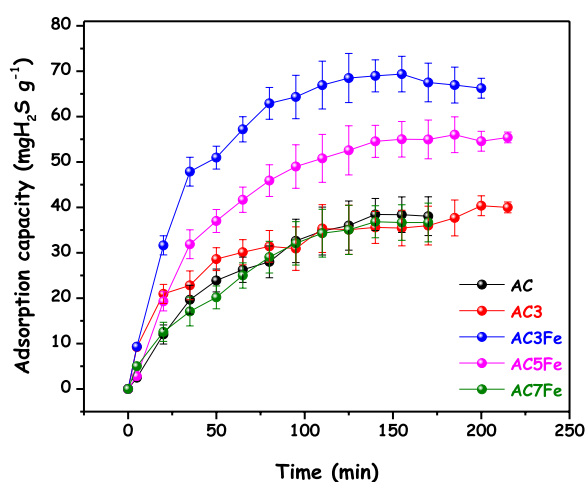


**Fig. 8** Kinetic curves obtained by GC analysis (headspace) indicating the  $\text{H}_2\text{S}$  adsorption capacities and the equilibrium time ranging from 150 to 250 min. The calculations are in accordance with Eq. (2)

contributed to the feasibility of the  $\text{H}_2\text{S}$  adsorption. However, under more drastic thermal treatment conditions, this material has a small contribution from the structure of the original activated carbon.

The adsorption capacities of the materials were calculated based on  $\text{H}_2\text{S}$  removal as a function of time (Fig. 8). The materials AC, AC3, and AC7Fe presented similar  $\text{H}_2\text{S}$  adsorption capacities, reaching 38.1, 40.0, and 37.9  $\text{mgH}_2\text{S g}^{-1}$  of adsorbent, respectively.

A preliminary analysis considering only the average deviation indicates that these results are equivalent and

confirm that the modification caused by the thermal treatment in the absence of iron, that is, gain in micro/mesopore area and micro/mesopore volume, did not favor a significant increase in the adsorption capacity for AC3.

Indeed, the results obtained from textural analysis and EDS analysis provided relevant information on the performance of the studied materials. For instance, the AC7Fe seems to have offset its specific area and micro/mesopore volume losses with the high concentration of iron species on its surface because its adsorption capacity was similar to those materials with higher specific area and micro/mesopore volume (AC and AC3). The iron-impregnated materials AC5Fe and AC3Fe showed a greater slope of the kinetic curve and, consequently, a higher desulfurization capacity than the first group (AC, AC3, and AC7Fe), ranging from 52.1 to 66.3  $\text{mgH}_2\text{S g}^{-1}$  of adsorbent. These results are approximately 37 and 74% higher than the one obtained for AC, respectively. Although a deeper study to identify what iron species were formed on the AC surface upon thermal treatment was not carried out, these results confirm our expectation regarding boosting the activity of the AC porous surface. Moreover, this suggests that the higher surface area and micro/mesopore volume of iron-containing AC3Fe were not the only reasons for a superior  $\text{H}_2\text{S}$  removal performance because AC3, which also showed a gain in the specific area and micro/mesopore volume, had more discreet performance in desulfurization, reaching only 40.0  $\text{mgH}_2\text{S g}^{-1}$ . In addition, the material AC5Fe, which presented a relatively lower specific

area ( $317.2 \text{ m}^2 \text{ g}^{-1}$ ) and high iron content, showed an  $\text{H}_2\text{S}$  removal only  $\sim 27\%$  lower than those obtained for AC3Fe, suggesting once again the relevant role of the iron species for  $\text{H}_2\text{S}$  removal. Indeed, the adsorbent's carbonaceous matrix received an activation boost due to a simultaneous combined effect between improving its textural properties (increase in specific area and micro/mesopore volume, Table 2), and formation of sites containing iron species (Fig. 4). As a first insight, iron species might have had their oxidizing power increased because the heat would have favored its attack on the activated carbon wall, causing a partial collapse of the carbonaceous matrix (abrasion, appearance of new pores, and interconnection of blind and closed pores to open ones) and formation of active sites as iron species found suitable places to settle down. Comparatively, a negative aspect concerning AC5Fe and AC7Fe is that, although they had high performances, the great weight loss depicted during thermal treatment ( $\sim 75\text{--}79\%$ , Table 1) makes their use unfeasible, that is, the only material that shows technical viability is AC3Fe. According to the literature, the adsorption capacity of activated carbons can vary intensely but usually ranges from 20 to  $40 \text{ mg g}^{-1}$  for ordinary commercial activated carbon and can reach  $210 \text{ mg g}^{-1}$  or more for modified ones (Yan et al. 2002; Sitthikhankaew et al. 2011). However, literature usually reports adsorption capacities obtained in continuous flow fixed bed columns. Therefore, due to the special confinement conditions achieved in the static system, the adsorption capacity of the materials studied in this work may be lowered if evaluated in a continuous flow system. Despite that, the analytical method worked well for comparative purposes between modified activated carbon and non-modified one submitted to the same experimental conditions.

Table 3 shows the results obtained from the single-factor ANOVA analyses considering the performances of the modified and non-modified activated carbons. The first analysis was performed with a complete

dataset containing the five materials. The obtained p-value 0.005155 ( $< 0.05$ ) allows to reject the null hypothesis and confirm the distinction between the adsorption capacities. In order to evaluate the behavior of the material AC5Fe (pink line in Fig. 8), a second dataset was considered without the AC3Fe material and the p-value increased to 0.055737 ( $> 0.05$ ), indicating that, statistically, the adsorption capacity of the AC5Fe material cannot be clearly distinct from others. In fact, the p-value is slightly higher than the established limit of 0.05. A third analysis was performed without samples AC3Fe and AC5Fe (not included in Table 3) and the p-value found was 0.941795 ( $> 0.05$ ), confirming that the materials AC, AC3 and AC7Fe presented practically the same performance for  $\text{H}_2\text{S}$  removal.

In order to get an insight into the adsorption process and mainly the different performances displayed by the studied materials, three kinetic models were used to assess the fit of the experimental data. Figure 9 shows the result of fitting the nonlinear models to the studied materials. All materials had their data fitted to three kinetic models and showed good linear correlation ( $R^2$ ). However, the pseudo-first order (PFO) model was the one that showed the closest proximity between experimentally determined adsorption capacity ( $q_{\text{exp}}$ ) and calculated adsorption capacity ( $q_{\text{calc}}$ ). Bangham's model, a derivation of the PFO model, was included to verify if the microporosity of the materials could have interfered with the adsorption process. Additionally, the pseudo-second order model (PSO) was used to evaluate if the presence of iron adsorption sites could have favored a second-order mechanism. Table 4 presents the kinetic parameters obtained for all the materials; for PFO and Bangham's models, all  $q_{\text{exp}}$  were very close to  $q_{\text{calc}}$ . Conversely, the PSO model showed a significant deviation between  $q_{\text{exp}}$  and  $q_{\text{calc}}$ , presenting a trend toward a steeper slope of the curve and a supposedly higher adsorption capacity, which is inconsistent with the observed results. The depicted behavior indicates that, despite the intense

**Table 3** Single-factor ANOVA analysis for the materials performance results

Source of variation	SQ	Df	Mean Sq	F-value	p-value	F-critical
<i>Dataset (All samples)</i>						
Intergroups	1498.266	4	374.5665	15.34681	0.005155	5.192168
Intragroups	122.034	5	24.4068			
Total	1620.30	9				
<i>Dataset (without AC3Fe)</i>						
Intergroups	518.958	3	172.986	6.158606	0.055737	6.591382
Intragroups	112.354	4	28.0885			
Total	631.312	7				

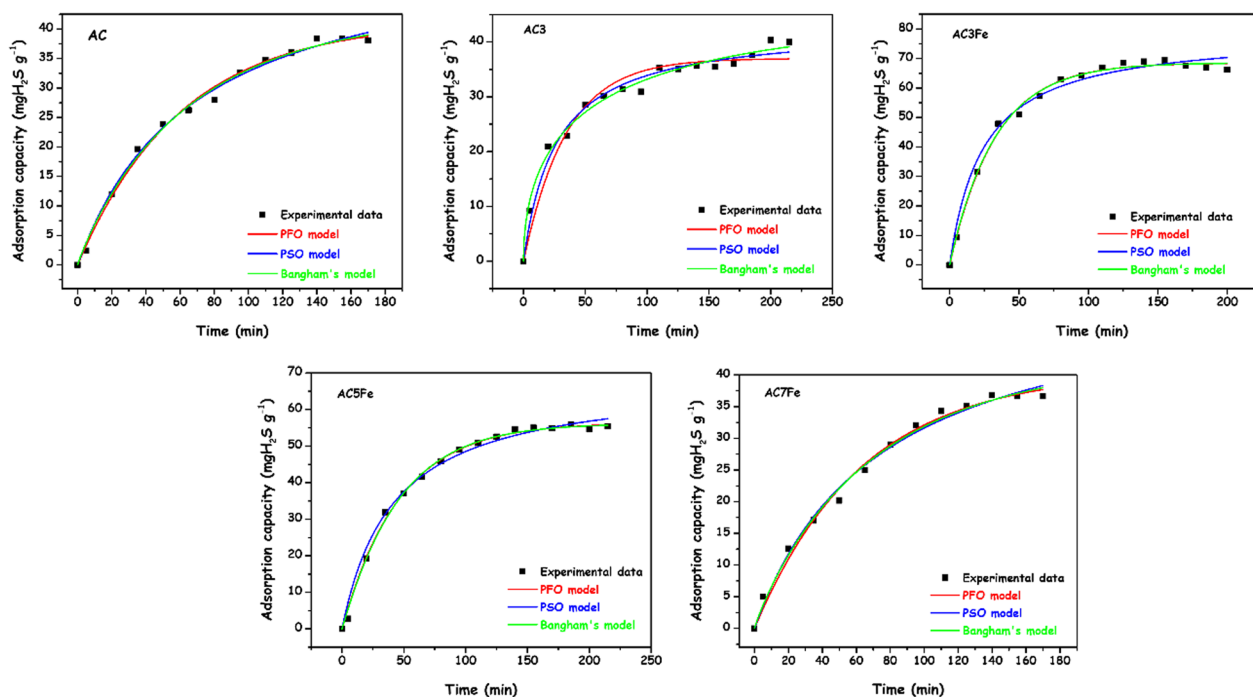


**Fig. 9** Fittings of nonlinear models pseudo-first-order, pseudo-second-order and Bangham’s model performed in each experimental kinetic curve

**Table 4** Kinetic parameters obtained for the ACs studied using three different models

Sample ID	PFO model				PSO model			Bangham’s model		
	$q_{exp}$	$q_{calc}$	$k_1 (\times 10^{-2})$	$R^2$	$q_{calc}$	$k_2 (\times 10^{-4})$	$R^2$	$q_{calc}$	$k_b (\times 10^{-2})$	$R^2$
AC	38.1	41.2	1.65	0.999	55.4	2.63	0.999	42.7	2.05	0.999
AC3	40.0	36.9	2.88	0.999	42.8	8.83	0.999	46.0	11.8	0.999
AC3Fe	66.3	68.5	3.04	0.999	78.8	5.27	0.999	68.5	3.20	0.999
AC5Fe	52.1	56.4	2.16	0.999	68.5	3.53	0.999	56.2	2.00	0.999
AC7Fe	37.0	40.5	1.58	0.999	55.0	2.46	0.999	42.4	2.04	0.999

$q_{exp}$  = experimental adsorption capacity ( $mg\ g^{-1}$ )

$q_{calc}$  = calculated adsorption capacity ( $mg\ g^{-1}$ )

$k_1$  and  $k_b$  = rate constant for PFO and Bangham’s models, respectively, ( $min^{-1}$ )

$k_2$  = rate constant for PSO model ( $mg\ g^{-1}\ min^{-1}$ )

PFO pseudo-first-order model, PSO pseudo-second-order model

thermal treatment performed on the ACs, especially in the presence of iron species, the adsorption mechanism did not change significantly for each modified material, and the PFO model satisfactorily represents the adsorption dynamics, that is, a mechanism predominantly based on the formation of multilayers of  $H_2S$  on the adsorbent’s surface. Notwithstanding, the good fitting presented by Bangham’s model may indicate the important role of the micropores comprising each material, which represents 68–71 wt% of the total specific area (Table 2).

Although the PFO model is closer to a physisorption process, literature suggests that ordinary activated

carbon surfaces contain oxygen-based groups that allow the formation of highly exothermic bonds regarding complexes between  $H_2S$  and C-O, indicating that this process can be ruled by chemisorption (Kazmierczak-Razna 2015; Li et al. 2016). The results presented in Table 4 suggest that the non-modified AC material follows the same trend as the modified ones, possibly as an effect of coexistence of chemi- and physisorption processes due to the intrinsic characteristics of this material, as aforementioned in XRD discussion, due to the presence of oxygen-based species. In the case of AC3Fe, AC5Fe and AC7Fe, it is possible to infer that the thermal

treatment in the presence of iron species and an oxidizing atmosphere (air), which caused a more drastic oxidation, led to the increase of stronger and non-dissociative adsorption sites for H<sub>2</sub>S chemisorption (Shen et al. 2019), supporting a scenario of coexistence of physisorption and chemisorption.

Table 4 also reveals that the rate constant value for the adsorption involving the AC material is one of the lowest ( $k_1 = 1.65 \text{ min}^{-1}$ ), almost as low as that obtained for the AC7Fe ( $1.58 \text{ min}^{-1}$ ), which is a highly mineralized material, and practically half of that obtained for the AC3Fe material. Actually, this is opposite what would be expected if the reaction rate were dependent only on the type of adsorption site (i.e., weak attachment—physisorption; strong attachment—chemisorption); this seemingly contradictory information is explained by the fact that the adsorption kinetic on the studied ACs is ruled by both type of adsorption sites (presence of active species spread on its surface) and textural characteristics (mainly, specific area and pore volume). The gain in specific area and volume of pores containing iron active sites for H<sub>2</sub>S adsorption are responsible for the higher adsorption rate of the modified materials.

## Conclusion

Although activated carbon is one of the most known materials for adsorption purposes, surface modification is yet an alternative to improve its performance in separation processes. The modified materials showed higher specific area, pore volume, and iron species dispersed over its surface, which led to a significant increase in its adsorption capacity compared to the ordinary AC. The thermal treatment associated to iron(III) chloride allows mitigate the abrupt mineralization of the activated carbons and favored the formation of controlled microporosity. Both physical and chemical sorption may coexist until the saturation of the adsorbent's surface.

The static batch system used to evaluate H<sub>2</sub>S adsorption showed potential to be used as a technique for determining the adsorption capacity of an adsorbent material. However, the experimental arrangement requires adjustments to increase the level of reliability of the data collected. A clear advantage of the proposed method is to allow the use of a standard synthetic biogas mixture, which excludes fluctuations in the concentrations of gases that form biogas. Also, the use of standard gas mixture in a continuous flow column could present an impeding cost for multiple long-term analysis. On the other hand, the proposed system is sensitive to the dilution step with the inert solid, to the transfer of gas aliquots between flasks, and moisture from air due to inefficient

evacuation. Nevertheless, this analytical method may be an alternative to measure total adsorption capacity of materials with potential for desulfurization.

## Abbreviations

[Fe(NCS)(OH <sub>2</sub> ) <sub>5</sub> ] <sup>2+</sup>	Pentaaqua(thiocyanate)iron(III)
μm	Micrometer
AC	Activated carbon
ALC	Aluminum cylinder type
ATR-FTIR	Attenuated total reflectance-Fourier transform infrared
BET	Brunauer–Emmett–Teller method
BJH	Barrett–Joyner–Halenda method
CH <sub>4</sub>	Methane
CO <sub>2</sub>	Carbon dioxide
CuO	Copper oxide
De Boer	De Boer method
DFT	Density functional theory
EDS	Energy-dispersive spectroscopy
FeCl <sub>3</sub> ·6H <sub>2</sub> O	Iron(III) chloride hexahydrate
GC	Gas chromatography
H <sub>2</sub>	Hydrogen
H <sub>2</sub> O	Water
H <sub>2</sub> S	Hydrogen sulfide
He	Helium
HNO <sub>3</sub>	Nitric acid
KSCN	Potassium thiocyanate
kV	Kilovolt
mA	Milliampere
min	Minute
N <sub>2</sub>	Nitrogen
O <sub>2</sub>	Molecular oxygen
PFO	Pseudo-first-order model
ppmv	Part per million in volume
PSA	Pressure swing adsorption
PSO	Pseudo-second-order model
PXRD	Powder X-ray diffraction analysis
qH <sub>2</sub> S	Adsorption capacity of hydrogen sulfide in a given adsorbent
RPM	Rotation per minute
S <sub>BET</sub>	Total specific area
SEM	Scanning electron microscopy
S <sub>ext</sub>	Specific area for external surface
S <sub>micro</sub>	Specific area for micropores
SO <sub>x</sub>	Sulfur oxide
TCD	Thermal conductivity detector
UV–Vis	Ultraviolet–visible spectroscopy
ZnO	Zinc oxide

## Acknowledgements

The authors acknowledge the financial support obtained from Novos Arranjos de Pesquisa e Inovação em Hidrocarbonetos Renováveis (NAPI-HCR) from Araucaria Foundation (grant agreement 006/2021– NAPI-HCR project), and Conselho Nacional de Desenvolvimento Científico e Tecnológico (CNPq, Grants 420097/2021-0, 307505/2021-9). They are also thankful to the Multiuser Laboratory of Federal University of Technology—Paraná—Campus Londrina—for the performed analyses, as well as for the biogas cylinder and gas recharge gently donated by Buschle & Lepper Company.

## Author contributions

MEAM performed adsorption experiments, GC analysis, and data interpretation; LE performed BET analysis and data interpretation; CLBG contributed with conceptualization of the idea; GGCA participated on draft writing; RMG performed FTIR analysis, results discussion, final manuscript writing; PHYC contributed with original draft and experiments conceptualization; CRTT contributed with the final text review; AB is the responsible for the research project, student guidance, and performed the draft and final text writing and discussion. All authors read and approved the final manuscript.



## Funding

This study was funded by NAPI-HCR from Araucaria Foundation (grant agreement 006/2021– NAPI-HCR project); Conselho Nacional de Desenvolvimento Científico e Tecnológico (CNPq, Grants 420,097/2021-0, 307,505/2021-9).

## Availability of data and materials

The datasets used and/or analyzed during the current study are available from the corresponding author on reasonable request.

## Declarations

## Competing interests

The authors report there are no competing interests to declare.

## Author details

<sup>1</sup>Grupo de Química de Materiais e Tecnologias Sustentáveis (GQMATS), Universidade Tecnológica Federal Do Paraná (UTFPR), Londrina, Paraná CEP: 86036-370, Brazil. <sup>2</sup>Departamento de Química, Universidade Estadual de Londrina (UEL), Londrina, Paraná CEP: 86050-482, Brazil. <sup>3</sup>Departamento de Química, Universidad de Guadalajara (UDG), CP: 44430, Guadalajara, Jalisco, Mexico. <sup>4</sup>Departamento de Química, Universidade Tecnológica Federal Do Paraná (UTFPR), Medianeira, Paraná CEP: 85884-000, Brazil. <sup>5</sup>Departamento de Engenharia Química, Universidade Tecnológica Federal Do Paraná (UTFPR), Londrina, Paraná CEP: 86036-370, Brazil.

Received: 9 December 2023 Accepted: 27 March 2024

Published online: 16 April 2024

## 7. References

- Agilent (2023) Database for chromatographic analysis. <https://www.chem.agilent.com/cag/CABU/cgramh.htm>. Accessed 01 December 2023.
- ANP - National Agency for Petroleum, Natural Gas and Biofuels - Brazil. Resolution nº 685/2017. <https://www.gov.br/anp/pt-br/assuntos/producao-e-fornecimento-de-biocombustiveis/biometano>
- Ardolino F, Cardamone GF, Parrillo F, Arena U. Biogas-to-biomethane upgrading: a comparative review and assessment in a life cycle perspective. *Renew Sustain Energ Rev*. 2021;139: 110588. <https://doi.org/10.1016/j.rser.2020.110588>.
- Barbera E, Menegon S, Banzato D, D'Alpaos C, Bertuccio A. From biogas to biomethane: a process simulation-based techno-economic comparison of different upgrading technologies in the Italian context. *Renew Energ*. 2019;135:663–73. <https://doi.org/10.1016/j.renene.2018.12.052>.
- Barrett EP, Joyner LG, Halenda PP. The determination of pore volume and area distributions in porous substances. I. Computations from nitrogen isotherms. *J Am Chem Soc*. 1951;73(1951):373–80. <https://doi.org/10.1021/ja01145a126>.
- Barroso-Bogeat A, Alexandre-Franco M, Fernández-González C, Gómez-Serrano V. Activated carbon surface chemistry: changes upon impregnation with Al(III), Fe(III) and Zn(II)-metal oxide catalyst precursors from NO<sub>3</sub><sup>-</sup> aqueous solutions. *Arab J Chem*. 2019;12:3963–76. <https://doi.org/10.1016/j.arabj.2016.02.018>.
- Becker CM, Marder M, Junges E, Konrad O. Technologies for biogas desulfurization - An overview of recent studies. *Renew Sustain Energ Rev*. 2022;159: 112205. <https://doi.org/10.1016/j.rser.2022.112205>.
- Bedia J, Peñas-Garzón M, Gómez-Avilés A, Rodríguez JJ, Belver C. Review on activated carbons by chemical activation with FeCl<sub>3</sub>. *J Carbon Res*. 2020;6:21. <https://doi.org/10.3390/c6020021>.
- Bezerra DP, Oliveira RS, Vieira RS, Cavalcante CL Jr, Azevedo DCS. Adsorption of CO<sub>2</sub> on nitrogen-enriched activated carbon and zeolite 13X. *Adsorption*. 2011;17:235–46. <https://doi.org/10.1007/s10450-011-9320-z>.
- Bhattacharjya D, Jong-Song Y. Activated carbon made from cow dung as electrode material for electrochemical double layer capacitor. *J Power Sources*. 2014;262:224–31. <https://doi.org/10.1016/j.jpowsour.2014.03.143>.
- Bian C, Gao Q, Zhang J, Xu Y, Liu Q, Qian G. Impact of pyrone group on H<sub>2</sub>S catalytic oxidation. *Sci Total Environ*. 2019;695: 133875. <https://doi.org/10.1016/j.scitotenv.2019.133875>.
- Bläker C, Muthmann J, Pasel C, Bathen D. Characterization of activated carbon adsorbents—state of the art and novel approaches. *ChemBioEng Reviews*. 2019;6:119–38. <https://doi.org/10.1002/cben.201900008>.
- Boldrin P, Ruiz-Trejo E, Mermelstein J, Menéndez JMB, Reina TR, Brandon NP. Strategies for carbon and sulfur tolerant solid oxide fuel cell materials, incorporating lessons from heterogeneous catalysis. *Chem Rev*. 2016;116:13633–84. <https://doi.org/10.1021/acs.chemrev.6b00284>.
- Brunauer S, Emmett PH, Teller E. Adsorption of gases in multimolecular layers. *J Am Chem Soc*. 1938;60:309–19. <https://doi.org/10.1021/ja01269a023>.
- Calbry-Muzyka A, Madi H, Rüschi-Pfund F, Gandiglio M, Biollaz S. Biogas composition from agricultural sources and organic fraction of municipal solid waste. *Renew Energ*. 2022;181:1000–7. <https://doi.org/10.1016/j.renene.2021.09.100>.
- Chang Q, Lin W, Ying W-c. Preparation of iron-impregnated granular activated carbon for arsenic removal from drinking water. *J Hazard Mater*. 2010;184:515–22. <https://doi.org/10.1016/j.jhazmat.2010.08.066>.
- Cheremisina OV, Ponomareva MA, Bolotov VA, Osipov AS, Sitko AV. Thermodynamic characteristics of the hydrogen sulfide sorption process by ferromanganese materials. *ACS Omega*. 2022;7:3007–15. <https://doi.org/10.1021/acsomega.1c06037>.
- Choudhury A, Lansing S. Adsorption of hydrogen sulfide in biogas using a novel iron-impregnated biochar scrubbing system. *J Environ Chem Eng*. 2021;9: 104837. <https://doi.org/10.1016/j.jece.2020.104837>.
- Cimino S, Lisi L, Erto A, Deorsola FA, de Falco G, Montagnaro F, Balsamo M. Role of H<sub>2</sub>O and O<sub>2</sub> during the reactive adsorption of H<sub>2</sub>S on CuO-ZnO/activated carbon at low temperature. *Microporous Mesoporous Mater*. 2020;295: 109949. <https://doi.org/10.1016/j.micromeso.2019.109949>.
- De Boer JH, Lippens BC, Linsen BG, Broekhoff JCP, van den Heuvel A, Osinga ThJ. The t-curve of multimolecular N<sub>2</sub>-adsorption. *J Colloid Interface Sci*. 1966;21:405–14. [https://doi.org/10.1016/0095-8522\(66\)90006-7](https://doi.org/10.1016/0095-8522(66)90006-7).
- Dumont E. H<sub>2</sub>S removal from biogas using bioreactors: a review. *Int J Energy Environ*. 2015;6:479–98.
- Egger F, Hülsen T, Batstone DJ. Continuous H<sub>2</sub>S removal from biogas using purple phototrophic bacteria. *Chem Eng J*. 2023;454: 140449. <https://doi.org/10.1016/j.cej.2022.140449>.
- Fahmi AG, Abidin Z, Kusmana C, Kharisma D, Prajaputra V, Rahmawati WR. Preparation and characterization of activated carbon from palm kernel shell at low temperature as an adsorbent for methylene blue. *IOP Conf Ser Earth Environ Sci*. 2019;399: 012015. <https://doi.org/10.1088/1755-1315/399/1/012015>.
- Ganash EA, Al-Jabarti GA, Altuwirqi RM. The synthesis of carbon-based nanomaterials by pulsed laser ablation in water. *Mater Res Express*. 2019;7: 015002. <https://doi.org/10.1088/2053-1591/ab572b>.
- Georgiadis AG, Charisiou ND, Gaber S, Polychronopoulou K, Yentekakis IV, Goula MA. Adsorption of hydrogen sulfide at low temperatures using an industrial molecular sieve: an experimental and theoretical study. *ACS Omega*. 2021;6:14774–87. <https://doi.org/10.1021/acsomega.0c06157>.
- Illathukandy B, Saadabadi SA, Kuo P-C, Wasajja H, Lindeboom REF, Vijay VK, Aravind PV. Solid oxide fuel cells (SOFCs) fed with biogas containing hydrogen chloride traces: impact on direct internal reforming and electrochemical performance. *Elektrochim Acta*. 2022;433: 141198. <https://doi.org/10.1016/j.electacta.2022.141198>.
- Indayaningsih N, Destyorini F, Purawardi RI, Insiyanda DR, Widodo H. Production of activated carbon by using pyrolysis process in an ammonia atmosphere. *J Phys Conf Ser*. 2017;817: 012006. <https://doi.org/10.1088/1742-6596/817/1/012006>.
- Kalaruban M, Loganathan P, Nguyen TV, Nur T, Johir MAH, Nguyen TH, Trinh MV, Vigneswaran S. Iron-impregnated granular activated carbon for arsenic removal: application to practical column filters. *J Environ Manage*. 2019;239:235–43. <https://doi.org/10.1016/j.jenvman.2019.03.053>.
- Kazmierczak-Razna J, Gralak-Podemska B, Nowicki P, Pietrzak R. The use of microwave radiation for obtaining activated carbons from sawdust and their potential application in removal of NO<sub>2</sub> and H<sub>2</sub>S. *Chem Eng J*. 2015;269:352–8. <https://doi.org/10.1016/j.cej.2015.01.057>.
- Lecharlier A, Carrier H, Le Hécho I. Characterization of biogas and biomethane trace compounds: a critical review of advances in in situ sampling and preconcentration techniques. *Anal Chim Acta*. 2022;1229: 340174. <https://doi.org/10.1016/j.aca.2022.340174>.
- Li H, Zhu L, Wang J, Li L, Shih K. Development of nano-sulfide sorbent for efficient removal of elemental mercury from coal combustion fuel gas.

- Environ Sci Technol. 2016;50:9551–7. <https://doi.org/10.1021/acs.est.6b02115>.
- Li W, Xu C, Xie A, Chen K, Yang Y, Liu L, Zhu S. Microstructure study of phase transformation of quartz in potassium silicate glass at 900 °C and 1000 °C. *Crystals*. 2021;11:1481. <https://doi.org/10.3390/cryst11121481>.
- Luyckx M, Hausman J-F, Lutts S, Gea G. Silicon and plants: current knowledge and technological perspectives. *Front Plant Sci*. 2017;8:411. <https://doi.org/10.3389/fpls.2017.00411>.
- Ma X, Chen R, Zhou K, Wu Q, Li H, Zeng Z, Li L. Activated porous carbon with an ultrahigh surface area derived from waste biomass for acetone adsorption, CO<sub>2</sub> capture, and light hydrocarbon separation. *ACS Sustain Chem Eng*. 2020;8:11721–8. <https://doi.org/10.1021/acssuschemeng.0c03725>.
- Martins VMS, Sante LGG, Giona RM, Possetti GRC, Bail A. An inter-loop approach on hydrothermal carbonization of sewage sludge for the production of biochar and its application as an adsorbent for lead-acid battery recycling. *Clean Techn Environ Policy*. 2022;24:1639–52. <https://doi.org/10.1007/s10098-021-02269-8>.
- Okoro OV, Sun Z. Desulphurisation of biogas: a systematic qualitative and economic-based quantitative review of alternative strategies. *ChemEngineering*. 2019;3:76. <https://doi.org/10.3390/chemengineering3030076>.
- Ou HW, Fang ML, Chou MS, Chang HY, Shiao TF. Long-term evaluation of activated carbon as an adsorbent for biogas desulfurization. *J Air Waste Manag Assoc*. 2020;70:641–8. <https://doi.org/10.1080/10962247.2020.1754305>.
- Papurello D, Tomasi L, Silvestri S. Proton transfer reaction mass spectrometry for the gas cleaning using commercial and waste-derived materials: focus on the siloxane removal for SOFC applications. *Int J Mass Spectrom*. 2018;430:69–79. <https://doi.org/10.1016/j.jms.2018.05.002>.
- Papurello D, Gandiglio M, Kafashan J, Lanzini A. Biogas purification: a comparison of adsorption performance in D4 siloxane removal between commercial activated carbons and waste wood-derived char using isotherm equations. *Processes*. 2019;7:774. <https://doi.org/10.3390/pr7100774>.
- Pinto RLS, Vieira AC, Scarpetta A, Marques FS, Jorge RMM, Bail A, Jorge LMM, Corazza ML, Ramos LP. An overview on the production of synthetic fuels from biogas. *Bioresour Technol Rep*. 2022;18: 101104. <https://doi.org/10.1016/j.biteb.2022.101104>.
- Pires J, Fernandes R, Pinto ML, Batista M. Microporous volumes from nitrogen adsorption at 77 K: when to use a different standard isotherm? *Catalysts*. 2021;11:1544. <https://doi.org/10.3390/catal11121544>.
- Qu D, Yang Y, Lu K, Yang L, Li P, Yu J, Ribeiro AM, Rodrigues AE. Microstructure effect of carbon materials on the low-concentration methane adsorption separation from its mixture with nitrogen. *Adsorption*. 2018;24:357–69. <https://doi.org/10.1007/s10450-018-9951-4>.
- Shen F, Liu J, Gu C, Wu D. Roles of oxygen functional groups in hydrogen sulfide adsorption on activated carbon surface: a density functional study. *Ind Eng Chem Res*. 2019;58:5526–32. <https://doi.org/10.1021/acs.iecr.9b00507>.
- Sinha P, Banerjee S, Kar KK (2020). Characteristics of activated carbon. In: Kar K (ed) *Handbook of Nanocomposite Supercapacitor Materials I*. Springer Series in Materials Science, vol 300, Springer, pp 125–154. [https://doi.org/10.1007/978-3-030-43009-2\\_4](https://doi.org/10.1007/978-3-030-43009-2_4)
- Sitthikhankaew R, Predapitakkun S, Kiattikomol RW, Pumhiran S, Assabumrungrat S, Laosiripojana N. Comparative study of hydrogen sulfide adsorption by using alkaline impregnated activated carbons for hot fuel gas purification. *Energy Procedia*. 2011;9:15–24. <https://doi.org/10.1016/j.egypro.2011.09.003>.
- Tiwari P, Wang T, Indlekofer J, El Haddad I, Biollaz S, Prevot ASH, Lamkaddam H. Online detection of trace volatile organic sulfur compounds in a complex biogas mixture with proton-transfer-reaction mass spectrometry. *Renew Energy*. 2022;196:1197–203. <https://doi.org/10.1016/j.renene.2022.07.036>.
- Waters CL, Janupala RR, Mallinson RG, Lobban LL. Staged thermal fractionation for segregation of lignin and cellulose pyrolysis products: an experimental study of residence time and temperature effects. *J Anal Appl Pyrolysis*. 2017;126:380–9. <https://doi.org/10.1016/j.jaap.2017.05.008>.
- Yan R, Liang DT, Tsen L, Tay JH. Kinetics and mechanisms of H<sub>2</sub>S adsorption by alkaline activated carbon. *Environ Sci Technol*. 2002;36:4460–6. <https://doi.org/10.1021/es0205840>.
- Yang X, Lu D, Zhu B, Sun Z, Li G, Li J, Liu Q, Jiang G. Phase transformation of silica particles in coal and biomass combustion processes. *Environ Pollut*. 2022;292: 118312. <https://doi.org/10.1016/j.envpol.2021.118312>.
- Zhu HL, Papurello D, Gandiglio M, Lanzini A, Akpınar I, Shearing PR, Manos G, Brett DJL, Zhang YS. Study of H<sub>2</sub>S removal capability from simulated biogas by using waste-derived adsorbent materials. *Processes*. 2020;8:1030. <https://doi.org/10.3390/pr8091030>.
- Zulkefli NN, Azam AMIN, Masdar MS, Isahak WNRW. Adsorption–desorption behavior of hydrogen sulfide capture on a modified activated carbon surface. *Materials*. 2023;16:462. <https://doi.org/10.3390/ma16010462>.

## Publisher's Note

Springer Nature remains neutral with regard to jurisdictional claims in published maps and institutional affiliations.